Available online at https://link.springer.com/journal/42241
http://www.jhydrodynamics.com
Journal of Hydrodynamics, 2022
https://doi.org/10.1007/s42241-022-0034-3

Numerical investigation on the effects of current headings on vortex induced motions of a semi-submersible

Wei-wen Zhao[1], Zhi-yuan Wei[2], De-cheng Wan[1, 3*]
1. *Computational Marine Hydrodynamics Lab (CMHL), School of Naval Architecture, Ocean and Civil Engineering, Shanghai Jiao Tong University, Shanghai 200240, China*
2. *Marine Design & Research Institute of China, Shanghai 200011, China*
3. *Ocean College, Zhejiang University, Zhoushan 316021, China*

(Received April 26, 2022, Revised June 6, 2022, Accepted June 7, 2022, Published online June 20, 2022)

Abstract: In this paper, numerical simulations on vortex-induced motions (VIM) of a semi-submersible at two different current headings are conducted over a wide range of current velocities. The simulations are performed with the computational fluid dynamics (CFD) solver VIM-FOAM-SJTU which is an in-house solver developed based on the OpenFOAM framework. The turbulent flows are resolved with a shear stress transport-delayed detached eddy simulation (SST-DDES) model. Free decay tests for transverse and yaw motion are performed in calm still water to make sure the equivalent stiffness is setup correctly. Then the results of VIM, including motion response, forces and moments, and flow patterns are presented and analyzed carefully. Motions including transverse, in-line and yaw motion at different current headings and velocities are compared. Instantaneous vorticity in the wake regions at different time stamps are also illustrated for different current headings and velocities.

Key words: Vortex-induced motions (VIM), vortex-induced yaw, vim-FOAM-SJTU solver, Reynolds stress

Introduction

Modern floating offshore structures are usually characterized with increasing draft and low center of gravity to inhibit the heave motion, as a result of which a phenomenon named vortex-induced motions (VIM) becomes an important issue. Periodic vortex shedding alternates on each side the column structure immerged into the water, therefore pressure on the hull surface also changes periodicly, which furthermore causes oscillating horizontal motions. When the shedding frequency is quite close to the natural frequency, "lock-in" will occur in which the transverse motion is greatly amplified. This large horizontal motion will weaken the fatigue life of risers and mooring systems. Thus, it is critical to study the characteristics of VIM to help suppress platform motions and improve lifetime of risers and mooring systems.

Physical model test is one of the most commonly used method to investigate VIM, in which the Froude similitude is achieved to keep geometric and dynamic similarity between model and prototype. However, it is impossible to satisfy the Reynolds and Froude scaling simultaneously. The Reynolds numbers of prototype could reach supercritical level while the model tests usually at sub-critical, which may lead to different flow regime[1]. Finnigan and Roddier[2-3] conducted model tests of Spar at supercritical Reynolds number in six-degree-of-freedom (6DOF) for the first time to investigate the scale effect of VIM. It was found that VIM response of subcritical Reynolds numbers were relatively large at higher reduced velocities. Some field measurements have showed that the results were conservative compared with prototypes[4-5]. However, other factors may attribute to the dependency between the prototype and model tests, such as realistic current profile, damping, nonlinear stiffness, simplification of the risers and mooring systems and lack of accurate simulations for appendages in model tests[5-6]. Nevertheless, the results of model tests are still reliable enough to provide guidance on design for Spar and multi-column offshore platforms. The VIM of multi-column is more complex due to wake interaction among different

Project supported by the National Natural Science Foundation of China (Grant Nos. 51909160, 52131102 and 51879159), the National Key Research and Development Program of China (Grant No. 2019YFB1704200).
Biography: Wei-wen Zhao (1990-), Male, Ph. D.,
E-mail: weiwen.zhao@sjtu.edu.cn
Corresponding author: De-cheng Wan
E-mail: dcwan@sjtu.edu.cn

columns. Waals et al.[7] studied the effect of mass ratio, draft condition and pontoon on VIM for multi-column platforms. It was found that the flow induced motions were larger for lower mass ratio while inhibited by pontoons. Besides, large yaw responses were firstly observed for 0° current incidence at high reduced velocity at which galloping that the transverse motions became less regular might occur. Abundant experimental data were obtained from Goncçlves et al.[8-9] about the effect of current incidence and hull appendages on VIM for semi-submersible. It was showed that the largest transverse response had been observed for 45° while the largest yaw response happened for 0°. Liu et al.[10] has investigated the effect of pontoon and current incidence related to columns or platforms. It was observed that pontoon would inhibit the VIM of platform and the current incidence related columns have dominant effect on VIM. Gonçalves et al.[11] experimentally investigated the flow-induced motions on an array of four floating cylinders with low aspect ratio and compared the VIM response of different column geometry, distance between columns and current incident angles. The range of Reynolds number covered $10^4 < Re < 1.1\times10^5$. They also concluded that the existence of pontoons was responsible for a substantial decrease of the VIM amplitudes in the transverse direction. Modir et al.[12] conducted model tests of an elastically mounted square-section cylinder in towing tank at different current incident angles. It was observed that for 45° angle configuration, the VIM response is easy to have synchronization in a wider range of current velocities.

In recent years with the rapid development of computer science, computational fluid dynamics (CFD) has become an increasing powerful method for VIM research, which are superiorly characterized with theoretically unlimited computational domain and flexible setting for parametric studies. Chen and Chen[13] used finite-analytic Navier-Stokes (FANS) to study the VIM of semi-submersible with respect to scaling and rounded-corner effect. The results show that the scale effect is not evident while the VIM response is sensitive to corner rounding of columns. An overall hydrodynamics of semi-submersible in 45° current incidence was investigated by Liang and Tao[14] in which the forces and work done by each columns and pontoon were presented. It was found that the three upstream columns offer excitation loads while pontoon inhibits VIM. Moreover, the hysteresis of semi-submersible between force and motion was found and studied by tracing the development of flow pattern. CFD method also encourages the design and investigation for novel semi-submersibles to suppress VIM. Xu et al.[15] performed model tests and CFD simulations for heave and VIM suppressed (HVS) semi-submersible and it turned out that HVS had superior VIM response compared to conventional semi-submersible. Holland et al.[16] performed numerical simulation for a full scale semi-submersible with strakes on the columns. Zhao et al.[17] and Kim et al.[18] performed numerical studies on the VIM of a Paired-column semi-submersible designed by Houston Offshore Engineering. Liang et al.[19] performed a comprehensive numerical study on the VIM of a deep-draft semi-submersible and investigated the energy transformation of vortex shedding process. They also analyzed the corner shape effect on the flow characteristics and hydrodynamic loads. Liu et al.[20] studied the effect of base column on the VIM response of a circular cylinder with a low aspect ratio and established a relationship between the non-dimensional response amplitude and lift coefficient.

In this paper, numerical simulations of VIM for a semi-submersible with four square columns are carried out. Two different current incidences are studied to investigate the flow patterns when significant vortex induced motions (VIM) and vortex induced yaw motions (VIY) occur. Detailed methodology and computational setup are illustrated in the next section, followed by the presence and analysis of computational results of the motions, forces and flow patterns. Finally, some conclusions are summarized.

1. Numerical methods

In the present study, an OpenFOAM-based solver vim-FOAM-SJTU is utilized for all hydrodynamic simulations. The solver consists of a self-developed 6DOF module for solving motion, a mooring system module for solving the linear and nonlinear springs, a delay detached eddy simulation (DDES) module for solving the massive separating turbulent flows.

1.1 *Governing equations for fluid*

The fluid is assumed to be single-phase, incompressible, viscous, turbulent, and is governed by the following equations:

$$\nabla \cdot \boldsymbol{u} = 0 \tag{1}$$

$$\frac{\partial \boldsymbol{u}}{\partial t} + \nabla \cdot [(\boldsymbol{u} - \boldsymbol{u}_g)\boldsymbol{u}] - \nabla \cdot (\nu + \nu_t)\nabla \boldsymbol{u} = -\frac{1}{\rho}\nabla p \tag{2}$$

where $\boldsymbol{u}$ is velocity field, $\boldsymbol{u}_g$ is mesh velocity accounting for dynamic mesh motion, ρ is fluid density, ν and ν_t is the molecular and turbulent viscosity and p is pressure field.

1.2 *Turbulence modelling*

The DDES based on the two-equation shear stress transport (SST) model is utilized for the

turbulence modelling. In order to obtain the turbulent eddy viscosity, two extra transport equations should be solved:

$$\frac{\partial k}{\partial t}+\nabla\cdot[(\boldsymbol{u}-\boldsymbol{u}_g)k]=\tilde{G}-\beta^*k\omega+\nabla\cdot[(\nu+\alpha_k\nu_t)\nabla k] \tag{3}$$

$$\frac{\partial \omega}{\partial t}+\nabla\cdot[(\boldsymbol{u}-\boldsymbol{u}_g)\omega]=\gamma S^2-\beta\omega^2+\nabla\cdot[(\nu+\alpha_\omega\nu_t)\nabla\omega]+(1-F_1)CD_{k\omega} \tag{4}$$

where k and ω are the turbulent kinetic energy and specific dissipation rate to be solved, $\tilde{G}$ is the generation term for k equation, S is the invariant measure of velocity strain rate, $CD_{k\omega}$ is the cross-diffusion term for ω equation, F_1 is the first blending function for blending the k-ω, k-ε models and β^*, α_k, γ, β, α_ω are model constants.

After obtaining k and ω, the turbulent eddy viscosity is then calculated with the following formula

$$\nu_t=\frac{a_1k}{\max(a_1\omega,SF_2)} \tag{5}$$

where a_1 is another model constant, F_2 is the second blending function. Details about SST-DDES model can be referred to Zhao et al.[21].

1.3 *6DOF motion and dynamic deforming mesh*

The motion equations of the moving object are given by:

$$\dot{u}=\frac{X}{m}+vr-wq+x_g(q^2+r^2)-y_g(pq-\dot{r})-z_g(pr+\dot{q}),$$

$$\dot{v}=\frac{Y}{m}+wp-ur+y_g(r^2+p^2)-z_g(qr-\dot{p})-x_g(qp+\dot{r}),$$

$$\dot{w}=\frac{Z}{m}+uq-vp+z_g(p^2+q^2)-x_g(rp-\dot{q})-y_g(rq+\dot{p}),$$

$$\dot{p}=\frac{1}{I_x}\{K-(I_z-I_y)qr-m[y_g(\dot{w}-uq+vp)-z_g(\dot{v}-wp+ur)]\},$$

$$\dot{q}=\frac{1}{I_y}\{M-(I_x-I_z)rp-m[z_g(\dot{u}-vr+wq)-x_g(\dot{w}-uq+vp)]\},$$

$$\dot{r}=\frac{1}{I_z}\{N-(I_y-I_x)pq-m[x_g(\dot{v}-wp+ur)-y_g(\dot{u}-vr+wq)]\} \tag{6}$$

where X, Y and Z are the total forces of the object in the non-inertia frame, K, M and N are the total moments of the object in the non-inertia frame, x_g, y_g and z_g are the three components of the vector pointing from center of gravity to center of rotation. In the present study, the center of rotation is set to the same with center of gravity. Thus, the three components are zero. I_x, I_y and I_z are moment of inertia around three axes, m is the mass of the object. u, v, w, p, q and r are three linear and three angular velocities of the object in non-inertia frame. The dot above notation means the first order temporal derivative of corresponding velocity.

For the dynamic deforming mesh motion, the grid points are obtained by solving a Laplacian equation as

$$\nabla\cdot(\Gamma\nabla\mathbf{x}_g)=0 \tag{7}$$

where Γ is diffusion coefficient defined as the squared inverse distance between cell centre and moving boundary.

2. Simulation setup

2.1 *Geometry*

The geometry is a conventional semi-submersible which is a model tested in the RPSEA 5404 project. Table 1 gives principal parameters and dimensions of the semi-submersible and the side and top views of the semi-submersible are shown in Fig. 1 in which all the parameters are in prototype. The scale ratio of 1:54 is the same as the model test. Two current incidences, 0°, 45°, are tested and the schematics of array configurations are shown in Fig. 2 with respective characteristic length D of 0.406 m, 0.574 m.

2.2 *Reduced velocity*

The reduced velocity is one of the most important parameters for VIM and the definition is as below

$$U_r=\frac{UT_N}{D} \tag{8}$$

Table 1 Main particulars of the semi-submersible

Description	Quantity
Draft, H /m	44.2
Displacement, Δ /t	128 823
Main column span, B /m	71.9
Main column width, B_{col} /m	21.9
Column height, H_{col} / m	65.5
Pontoon width, B_{pon} /m	20.4
Pontoon height, H_{pon} /m	10.7
Column fillet radius, R /m	3.7
Yaw moment of Inertia, I_{zz} /(t·m^{-2})	1.953×10^{8}
Inline stiffness, K_x /(kN·m^{-1})	210
Transverse stiffness, K_y /(kN·m^{-1})	210
Yaw stiffness, K_{zz} /[(kN·m)·°$^{-1}$]	35 396

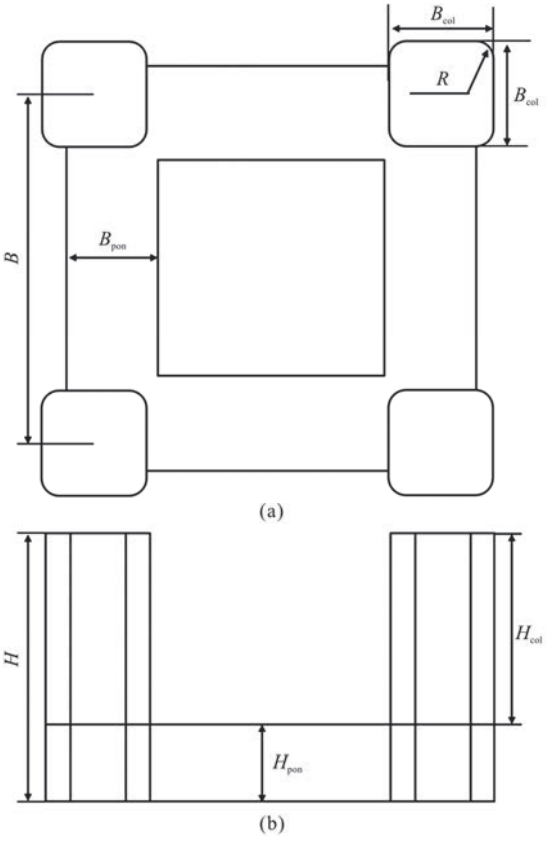

Fig. 1 Side and top view of the semi-submersible in prototype

where U is the towing velocity, T_N is the natural period obtained from the free decay tests. The range of reduced velocities simulated are 4-20 which corresponds to a Reynolds number range of 4.7×10^{4}-2.4×10^{5} but with a low Froude number up to 0.17. There is a statement in the RASEP project that the experiments were conducted with the same towing velocities ranging from 0.082 m/s-0.410 m/s for all current incidences but the statistical VIM results were based on the D of 45°. However, in this article the results are displayed according to respective D for each incidence therefore the range of reduced velocities are 5.6-21.2 for 0°, 4-15 for 45°.

2.3 *Mooring configuration*

Accurately simulating the mooring system is significant because the mooring stiffness will influence the natural period of semi-submersible and furthermore the calculation of reduced velocity. However, it is proved that what truly matters is not the configuration of the mooring lines but the equivalent stiffness matched to the model tests. In the present study, the equivalent stiffness is achieved with four fully pretensioned linear springs symmetrically layout around the platform (Fig. 2). The magnitude of pretension and spring stiffness is adjusted according to the equivalent stiffness and then is validated by the free decay tests in Section 3.1.

2.4 *Computational mesh and discretization schemes*

The computational domain shown in Fig. 3 is $12.4B\times6.8B\times4.5H$, which is large enough to eliminate the boundary effect. As for boundary conditions, a uniform current for velocity and zero gradient for pressure are set at the inlet while zero uniform for pressure and zero gradient for velocity are set at the outlet. The two lateral and the bottom sides are set to be symmetric as well as the top side due to the ignorance of the effect of the free surface at low Froude number, and a no-slip condition is set for the platform surface.

A hexahedron dominant mesh with octree refinement in some critical regions is employed throughout this study, as shown in Fig. 4. Both the initial background mesh and the refinement mesh near the wall and wake region are generated by the mesh generation tools of OpenFOAM. The background mesh generated by blockMesh has uniform grid spacing, based on which two refinement boxes covering the wake region are further generated by snappyHexMesh. The range of two boxes are $6.6B\times4B\times1.4H$, $4.8B\times2.8B\times1.4H$ with a mesh size of 0.101 m, 0.0506 m respectively. The boundary region of the platform surface is refined at a lever of 6 with 8 layers among which the mesh size at the first layer is 0.00106 m to ensure $y^{+}<1$ so that the flow separations and wake structures could be accurately captured. The total mesh number is approximately 3.09×10^{6}. The time step is set to 0.01 s for all the simulations.

The discretization schemes are as follow: the finite volume method for the governing equations, a three-level second order implicit scheme for the time, the linear upwind stabilized for transport (LUST) scheme for the convection of momentum equation, the

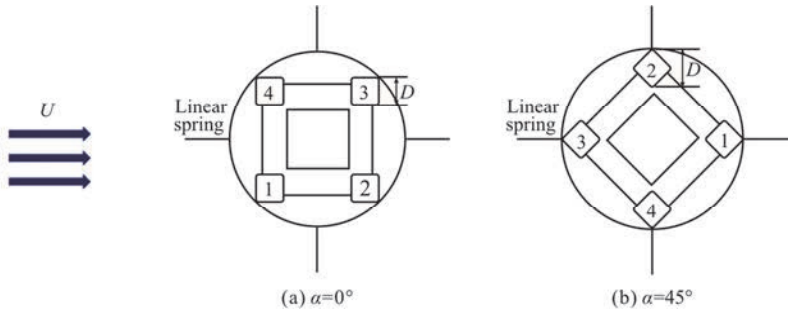

Fig. 2 Schematics of mooring systems, characteristic length and array configurations at α = 0°, 45°

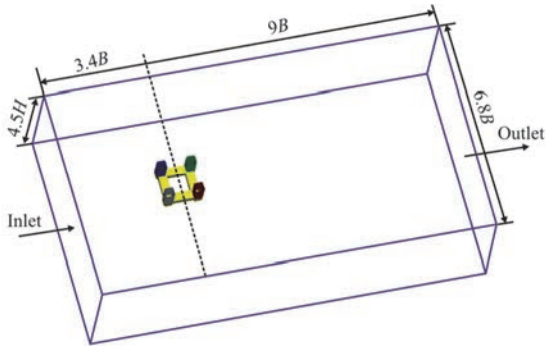

Fig. 3 (Color online) Computational domain

linear upwind scheme for the convection of turbulent transport equations, the Gauss linear for the diffusion. PIMPLE algorithm is employed to solve the coupling pressure and velocity problems. 3 inner corrections and 2 outer corrections are adopted for the PIMPLE algorithm.

3. Results and discussions

3.1 *Free decay*

Free decay tests are carried out by giving an initial velocity to the platform with only the corresponding freedom released in calm water and recording the time series, based on which the natural periods are obtained by frequency analyses. Since the mooring configurations and geometry properties of platform in transverse and in-line directions are symmetric, we only perform transverse and yaw decay tests here. Figure 5 gives out the time series and frequency results of transverse and yaw free decay test. Table 2 summarizes the natural periods of both CFD simulations and experimental fluid dynamics (EFD) tests, which proved that the numerical mooring configuration has effective stiffness as the experiment.

3.2 *Motion response*

The VIM responses in the present study are statistically proceeded and represented by the nominal response, which is a non-dimensional parameter defined as

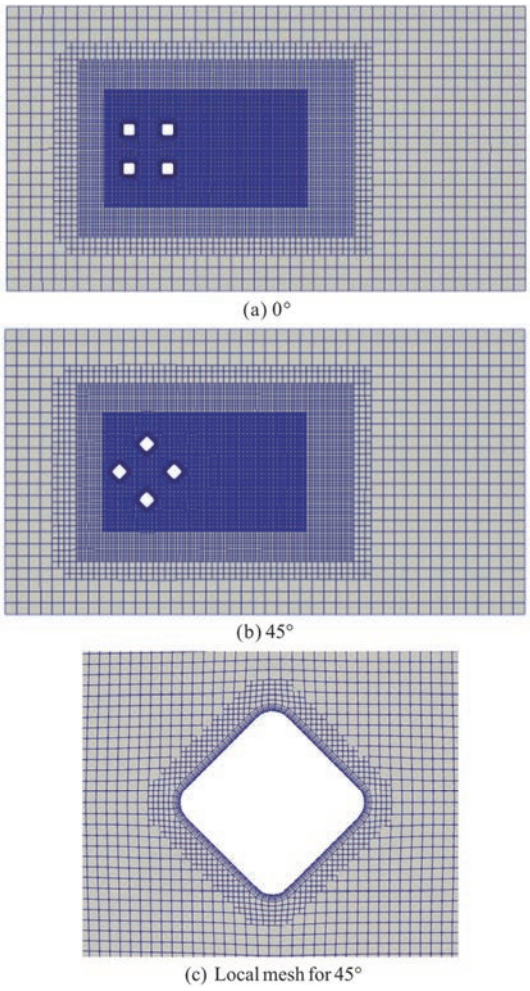

Fig. 4 (Color online) Computational mesh for different current headings

$$\left(\frac{A}{D}\right)_{\text{nominal}} = \frac{\sqrt{2}\sigma[Y(t)]}{D} \tag{9}$$

where A is the motion amplitude, $Y(t)$ is time series of motion response and σ is the standard derivation.

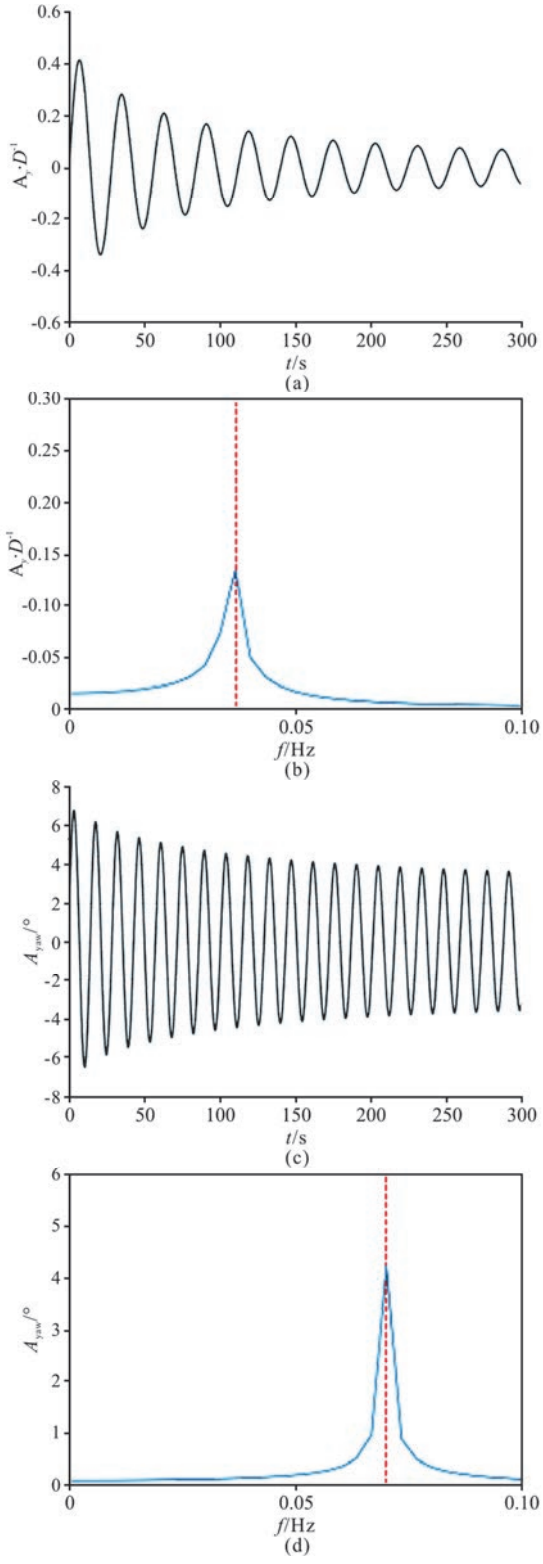

Fig. 5 (Color online) Time series and frequency results of transverse and yaw decay test

Figure 6 gives the results of nondimensional transverse amplitudes with corresponding reduced velocities at 0°, 45° current headings. The agreement between numerical study and experiment is overall satisfactory with exception of higher reduced velocity at 45°. The possible reason for the discrepancy may be due to the ignorance of nonlinear damping of mooring stiffness. It is shown that the transverse responses for 45° is over twice greater than those for 0°. The largest amplitudes occur at the range of $5 \le U_r \le 8$ for both current headings and these districts are so called "lock-in" range where the vortex shedding frequency is similar to the natural frequency (which can be seen from the fast Fourier transform (FFT) results in Fig. 11). However, the amplitudes drop sharply for 45° after the "lock-in" range while the amplitudes for 0° just become slightly lower and keep almost constant afterwards. It was mentioned by Waals et al.[7] that the galloping might happen at extremely high reduced velocities up to 15 when the vortex shedding periods would shift dramatically and the responses would increase monotonically. However, in this study, the highest reduced velocity is up to 21.2 for 0° but the galloping phenomenon is not confirmed herein.

Table 2 Natural periods of semi-submersible (in model scale)

Natural period/s	CFD	EFD	Error/%
T_x	27.98	28.58	2.09
T_y	27.98	28.58	2.09
T_{yaw}	14.40	12.93	11.37

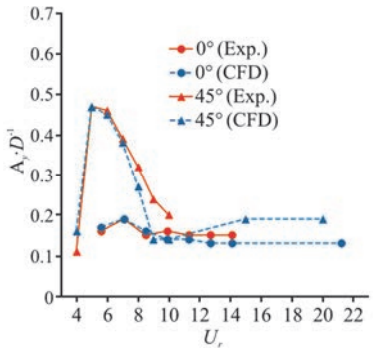

Fig. 6 (Color online) Nondimensional transverse responses for 0°, 45° current headings

Figure 7 shows the results of non-dimensional inline amplitudes for both 0°, 45° headings in which the average data is utilized. As can be seen, the platform offsets to the origin grow larger with velocities increasing. Additionally, the offset of 45° is larger than 0° and increase more sharply, which may be related to the layout of the columns so that the resistances of each columns differ. Further details will be shown through the flow pattern analysis in the following part.

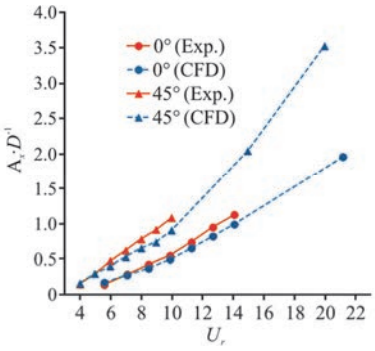

Fig. 7 (Color online) Non-dimensional inline responses for 0°, 45° current headings

Figure 8 presents the result of the yaw motions for two incidences. Due to limited statistic offered by experiment, the max amplitudes are compared and the tendency are consistent roughly. In contrast to the transverse response, the yaw motions for 0° is larger than 45° and the discrepancy grow larger with higher reduced velocities. Moreover, the peak response has not been obtained even at $U_r = 21.2$ for 0° and no "lock-in" phenomenon occurs at the corresponding range of transverse results. According to Waals et al.[7], the large yaw motions were as a consequence of the galloping phenomenon which however is not observed in this study as mentioned above. The yaw motions closely depend on the moments of the platform, therefore it can be inferred that the layout of each column for different current incidences will influence the vortex shedding regime and furthermore the moment of each column. It is suggested that the yaw motion is also related to yaw natural frequency and Fig. 9 re-calculates a new reduced velocities range based on the yaw natural period. It turns out that the velocity range for largest yaw motions is around $8 \le U_r \le 10$, which is closer to the VIM results for transverse, concluding that it is the yaw natural period but galloping could explain the yaw motions.

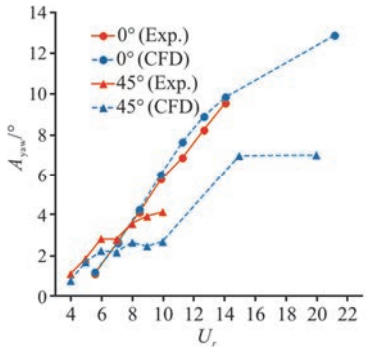

Fig. 8 (Color online) Yaw responses for 0°, 45° current headings

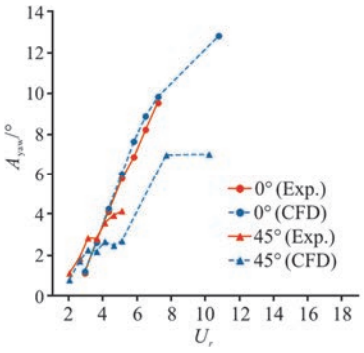

Fig. 9 (Color online) Yaw responses for 0°, 45° current headings with reduced velocities based on the yaw natural period

The FFT analyses of transverse and yaw motions are shown in Figs. 10, 11 in 3-D graphs with frequency versus reduced velocity versus amplitude. The red and blue line represents the natural frequency for transverse (inline) and yaw motions respectively and the dominant frequency corresponding to the peak amplitude is considered the shedding frequency. For transverse motions (Fig. 10) current incidences, concluding that the motions are enlarged due to the resonant effect of vortex shedding and platform motion. However, the distribution of dominant frequency for 45° is more concentrated and disappear when out of the lock-in range while the one for 0° transfer to the yaw natural frequency gradually with the peak amplitude less decreasing. It is suggested that the VIM motions for 0° might be the interaction of transverse and yaw motions or these two motions share the same excitation. The frequency results become irregular at extremely high reduced velocity without a dominant frequency found.

For yaw motions (Fig. 11), the frequency results perform quite different for 0°, 45°. The dominant frequency of largest amplitude occurs at the yaw natural frequency for 0°, which is similar to the regime of transverse motion. Instead, the frequency results of 45° feature less regular without an obvious dominant frequency even though there are some peaks around the yaw natural frequency. It is inferred that the resonance of 0° and the irregularity of 45° might be the consequence of different moment performances due to different vortex shedding interaction of each column, which is furthermore illustrated in the next part.

3.3 *Forces analysis*

The drag and lift forces of not only the whole platform but also each column and pontoon are analyzed to investigate the contribution and interaction to VIM. Additionally, the results of moments in

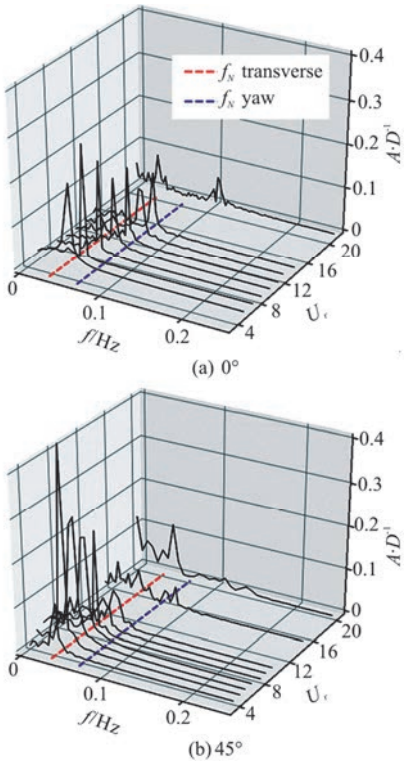

Fig. 10 (Color online) Frequency series of transverse motion responses

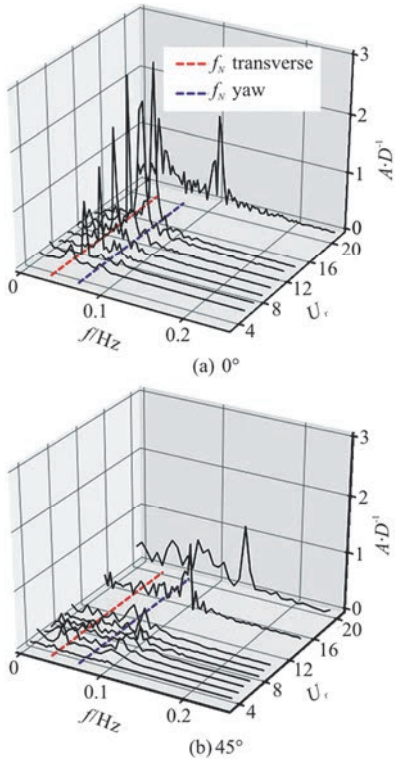

Fig. 11 (Color online) Frequency series of yaw motion responses

yaw direction are also researched to explain the different yaw performances for two incidences. Non-dimensional coefficients are utilized with definitions as follow:

$$C_D = \frac{F_D}{0.5\rho U^2 A_w} \tag{10}$$

$$C_L = \frac{F_L}{0.5\rho U^2 D A_w} \tag{11}$$

$$C_M = \frac{M_{zz}}{0.5\rho U^2 D^2 A_w} \tag{12}$$

where the F_D, F_L and M_{zz} represents the inline drag, transverse lift and yaw moment, A_w is the projected area of each part or platform for corresponding heading. All the results shown below are numerical statistic.

Figure 12 presents the drag results for 0°, 45° incidences. In general, the total drag is around 1.4-1.7 for 0°, 1.1-1.5 for 45° and the tendency of two total drag curves are both similar to transverse motions respectively, which suggests that the drag is influenced not only by current conditions but also transverse responses. The columns of port and starboard side (columns 1, 4 and columns 2, 3 for 0°, columns 2, 4 for 45°) perform good symmetry and the drag of back columns (columns 2, 3 for 0°, column 1 for 45°) are much smaller due to the shielding of front columns. Additionally, it is pontoon that contributes the largest percent to drag coefficient for both two headings.

Figures 13, 14 present the root mean square (rms) and mean lift coefficient for 0°, 45° current headings, respectively. In Fig. 13, the trend of all curves for 45° is quite similar to transverse motions and the three front columns (columns 2, 3 and 4) are nearly synchronous, suggesting the lift as the main excitation on transverse responses. However, as for 0°, the lift reaches the maximum at $U_r = 5.6$ but afterwards drops minimum abruptly at $U_r = 7.1$ while the peak and drop of transverse motions in Fig. 5 delay with a reduced velocity. This phenomenon is considered the hysteresis between the lift and transverse motions. The analysis on time series of each column at $U_r =$ 5.6, 7.1 shows that lifts at the former velocity are in phase while at the latter one almost out of phase. The symmetry of mean lift coefficient for 0° displayed in Fig. 14(a) suggests that the inner (near the center) and outer surfaces of each column may encounter different shear layer formation and reattachment so that the pressure distributions of two side of each column

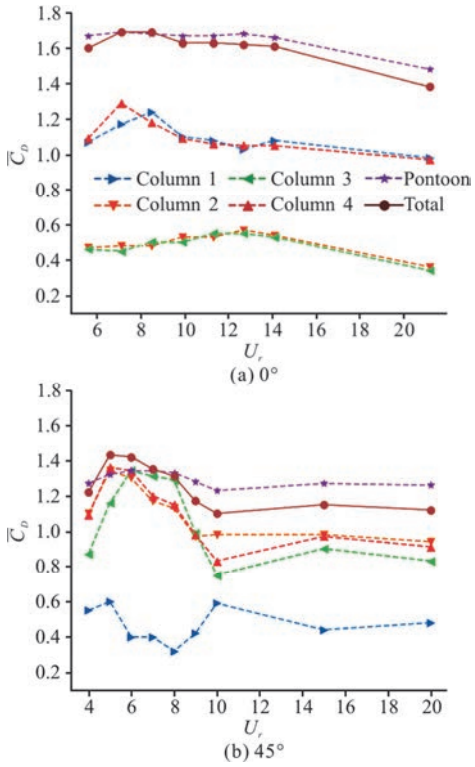

Fig. 12 (Color online) Numerical mean drag coefficient of platform and each part current headings

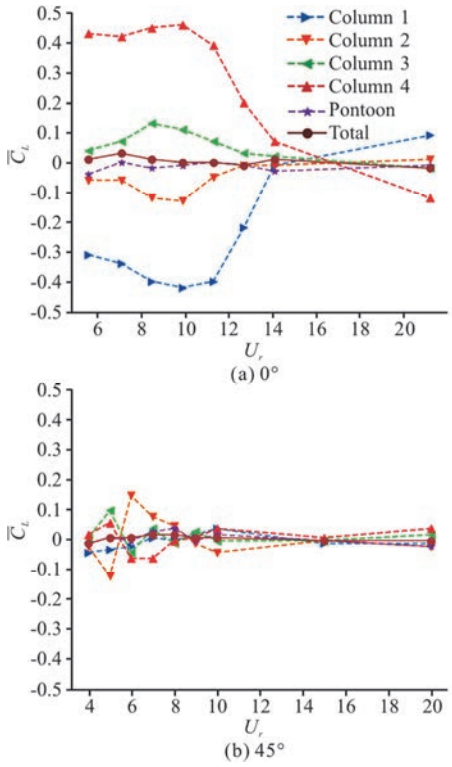

Fig. 14 (Color online) Mean lift coefficient of platform and each part current headings

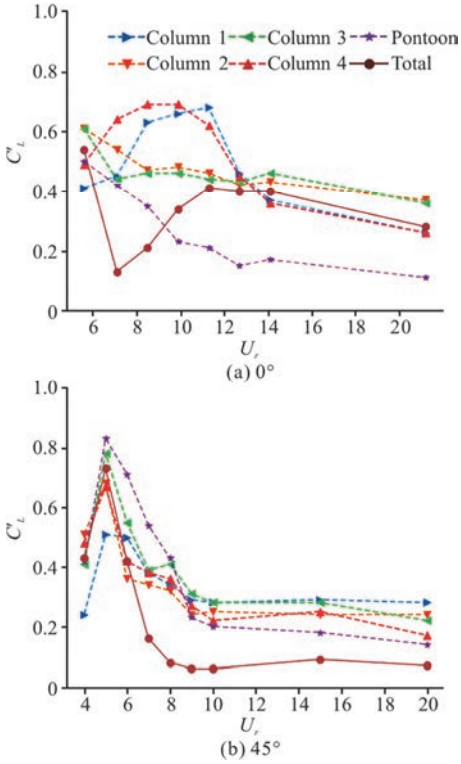

Fig. 13 (Color online) Root mean square lift coefficient of platform and each part current headings

differ, which might somewhat cause offset of lift effect and furthermore the transverse motions. On the other hand, for 45° the mean lift of each column is not quite symmetric about x-axis instead.

Figure 15 presents the moment coefficients in yaw direction. The results shows that moments of port and starboard columns for either 0° or 45° are significantly symmetric. The positive and negative deviation for symmetric columns might reveals the same reason as the mean lift results in Fig. 14. However, there are two pairs of symmetric deviation for 0° in deviation while there is only one pair for 45°, which probably demonstrates that the accumulation of yaw moment energy for 45° is less than 0°, leading to the smaller yaw responses.

3.4 *Flow patterns*

In this section, flow patterns are analyzed to further investigate the VIM mechanism of semi-submersible. Depending on reduced velocities, the flow patterns are organized into three distinctive groups for each incidence which include $U_r = 5.6$, 14.1 and 21.2 for $\alpha = 0°$, $U_r = 5$, 10 and 15 for $\alpha = 45°$ respectively. The first group which are given in Figs. 16, 17 corresponds to the max transverse motions situation. The second group given in Figs. 18, 19 represent the “post-lock-in” situation and the third

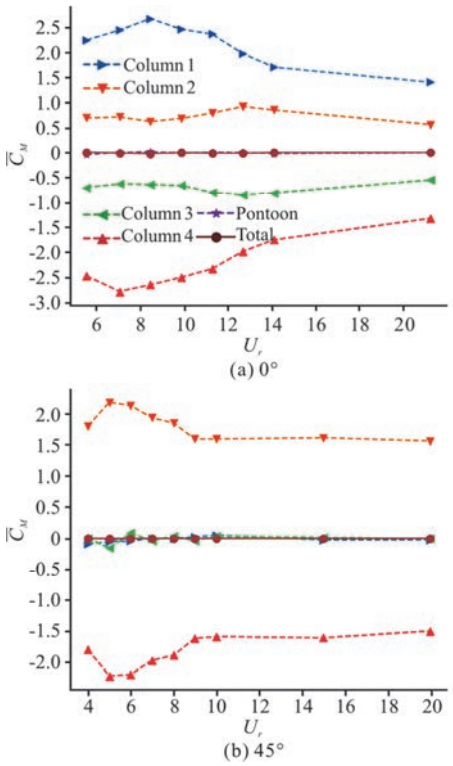

Fig. 15 (Color online) Numerical mean yaw moment coefficient of platform and each part current headings

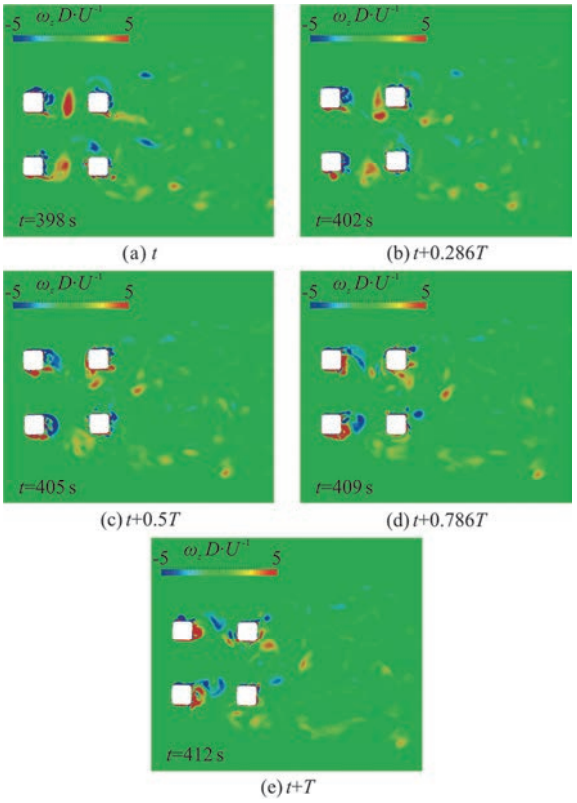

Fig. 16 (Color online) Sequential contours of Z vorticity for $\alpha = 0°$ at $U_r = 7.1$

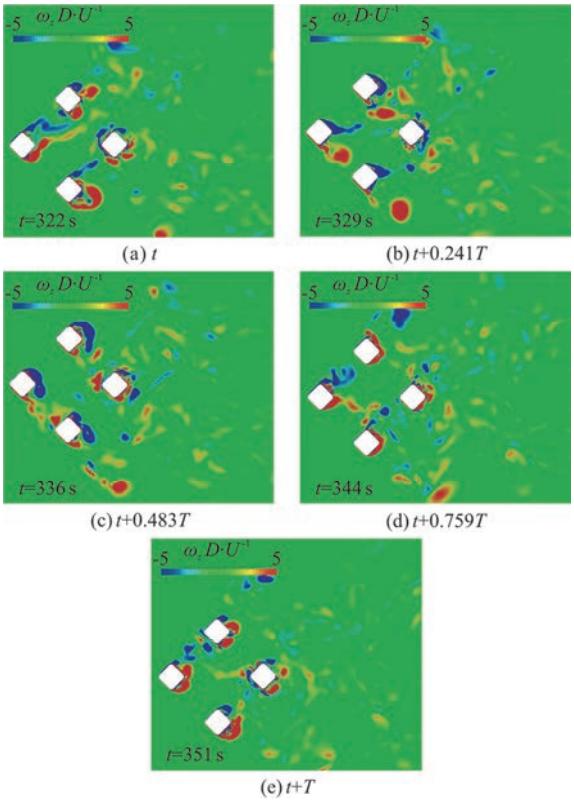

Fig. 17 (Color online) Sequential contours of Z vorticity for $\alpha = 45°$ at $U_r = 5$

one given in Figs. 20, 21 represent the max yaw motions situation. All 6 sets of results are displayed by the non-dimensional z component of vorticity $\omega_z D / U$ at the same horizontal plane $Z / H = -0.5$ in a figure with a periodic cycle series where the t is the instantaneous time, T is the transverse motion period.

The current velocity of the first group corresponds to $U_r = 7.1$ for $\alpha = 0°$, $U_r = 5$ for $\alpha = 45°$ respectively. It is observed in Figs. 16, 17 that the shear layers of the upstream columns (columns 1, 4 for 0°, columns 1, 2 and 4 for 45°) are attached to the surface of column for both current incidences, which will lead to larger pressure discrepancy between the bottom and top side so that the lift will also be enlarged. For $\alpha = 0°$, the vortex shedding of upstream columns is in-phase and occurs between the upstream and downstream columns. The downstream columns are immersed in the shedding wake without being impinged by the vortex structure directly and produce another vortex shedding in a smaller size. On the other hand, besides the in-phase shedding of three upstream columns for $\alpha = 45°$, the vortex structures tend to "hug back" the columns. It is probably the common effect of transverse motions and

the oblique room of the diamond shape before the vortex was crushed by such small current. The “hug back” structures make the pressure discrepancy even larger, not to mentioned there is one more column contributing to the lift for 45°, which explains that the lift coefficient and transverse motions at this velocity for 45° is much larger.

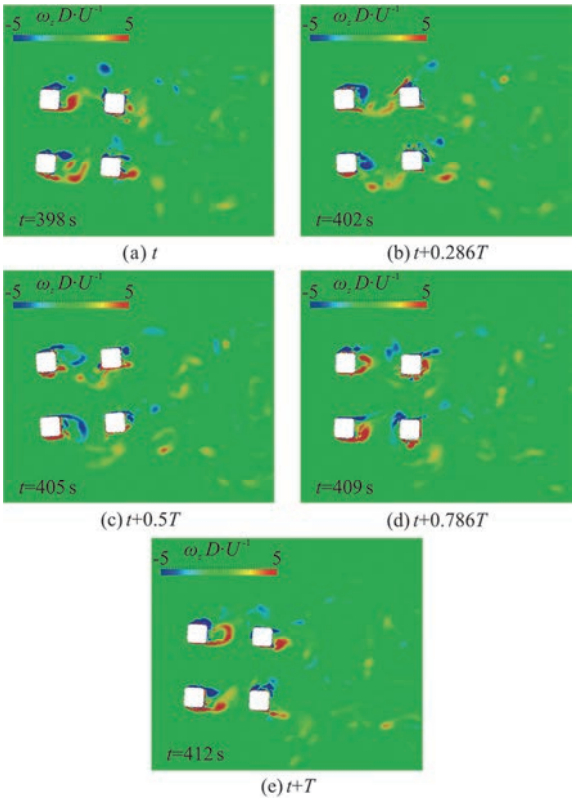

Fig. 18 (Color online) Sequential contours of Z vorticity for $\alpha = 0°$ at $U_r = 14.1$

In the second group, the reduced velocity is 14.1 for $\alpha = 0°$, 10 for $\alpha = 45°$ which is so called “post lock-in” stage where no more VIM is discovered for 45° while the transverse amplitude keeps almost constant for 0°. The vortex patterns for 0° in Fig. 18 is similar to the first group except that the vortex tends to shed relatively back and wag inside. Similarly, the vortex for 45° in Fig. 19 also grows narrower and the shedding from columns 2, 4 is almost anti-phase while the column 1 sometimes shed simultaneously with column 2 but sometimes with column 4. This shedding pattern makes the transverse motions complicated and consequently no clear dominant frequency exists.

Figures 20, 21 represent the reduced velocity of 21.2 for 0°, 15 for 45°, corresponding to the max yaw motions situation. Observing the 0° flow map, it is found that the vortex shedding of inner and outer surface on columns is quite different: the inner shear layer is attached to the surface of upstream columns and even stretch to the downstream columns while the outer shear layer separates at the front corner and stretch outside before shedding almost in front of downstream columns. This wake pattern makes the downstream almost shielded by the upstream. As for 45°, the shedding of column 1 remains alternative, different from those of column 2, 4 which sometimes are alternative but sometimes simultaneous. However, it is interesting to find that the instances of simultaneous vortex shedding exactly match the position where the max yaw motions occur while in the instances of alternative shedding, only transverse motions are observed. These two different shedding regimes will lead to different pressure distribution. The simultaneous one will increase the proportion of drag forces while the alternative one will increase the lift forces. Furthermore, comparing the Figs. 12-14, it can be inferred that the moments deriving from the drag forces are the main proportion, which make it sense that the yaw motions at $\alpha = 0°$ is larger than that at $\alpha = 45°$ because the drag arms are zero for columns 1, 3 at $\alpha = 45°$ while there are four columns contributing to the moments for $\alpha = 0°$.

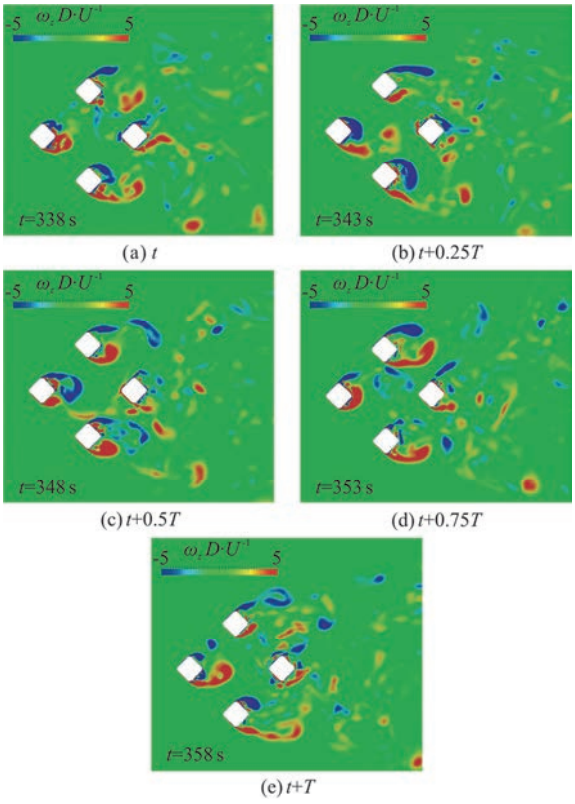

Fig. 19 (Color online) Sequential contours of Z vorticity for $\alpha = 45°$ at $U_r = 10$

4. Conclusions

In this paper, CFD simulations on VIM and VIY

of four columns semi-submersible at a model scale are carried out with VIM-FOAM-SJTU solver and two classical current incidences, 0°, 45°, are chosen with reduced velocities covering 4-22. The numerical results agree satisfactorily with model tests. Several conclusions are drawn as follow:

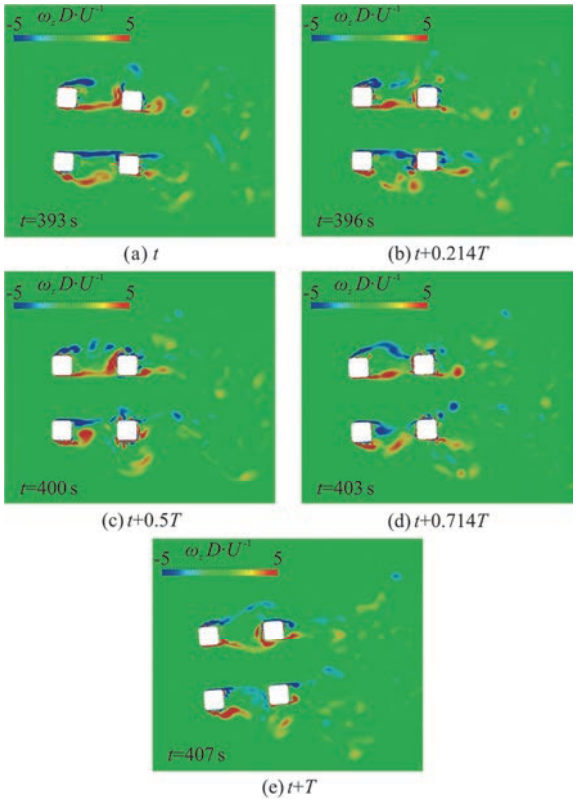

Fig. 20 (Color online) Sequential contours of Z vorticity for $\alpha = 0°$ at $U_r = 21.2$

The largest transverse motions occur at $U_r = 5$ for 45° and the peak distribution with reduced velocities is concentrated while the transverse amplitudes for 0° is small and flat. The inline amplitudes for 45° also varies more dramatically than 0°. Instead, it is found that the largest yaw motions occur at higher reduced velocity for 0° and the motions is closely related to yaw natural period. However, the "lock-in" phenomenon has not been observed yet.

The drag coefficient for 0° is slightly higher than 45° and rarely changes at higher velocities. Symmetry of lift and yaw moment is observed for the port and starboard columns for 0°, 45°. It is also shown that shear layer and vortex shedding regimes at the inner and outer surface of each column for 0° are different.

Through flow pattern analysis, a "hug back" vortex structure around the column for 45° is observed at the "lock-in" reduced velocity, making the pressure discrepancy between the top and bottom of columns larger. Moreover, in-phase vortex shedding of three upstream columns enlarges the transverse motions dramatically while out-of-phase shedding makes the motions complicated. On the other hand, the reattachment of shear layer and the vortex shedding for 0° is similar at each case due to the shielding distribution of upstream and downstream, explaining the flat changing for transverse motions. By combining the shedding evolution and the platform motions for 45°, it is found that the drag forces offers the main proportion of moments and the simultaneous vortex shedding from the top and bottom of the column leads to larger yaw motions. The drag arms of all columns for 0° are not zero, therefore there are four torque excitations to the center while there are only two columns for 45°, which explains why the moment of platform and yaw motions for 0° are larger.

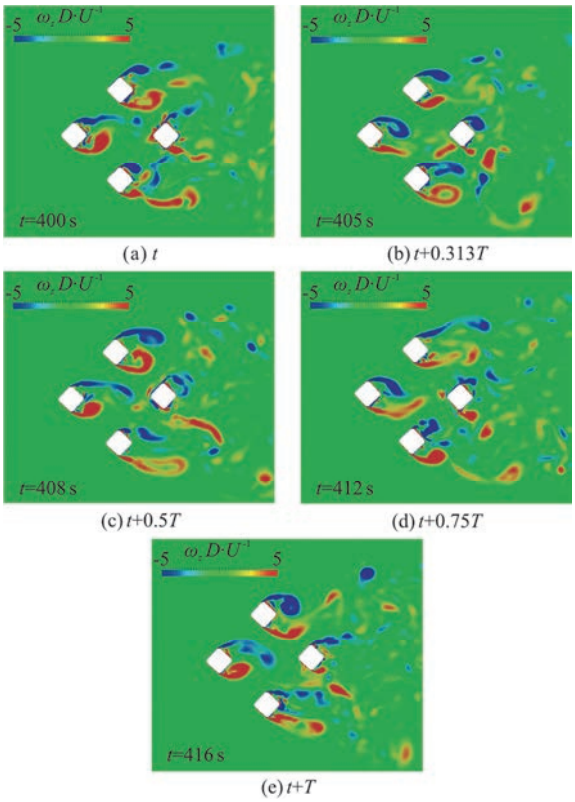

Fig. 21 (Color online) Sequential contours of Z vorticity for $\alpha = 45°$ at $U_r = 15$

References

[1] Rijken O., Leverette S. Experimental study into vortex induced motion response of semi submersibles with square columns [C]. *ASME 27th International Conference on Offshore Mechanics and Arctic Engineering*. Estoril, Portugal, 2008, 263-276.

[2] Finnigan T., Roddier D. Spar VIM model tests at supercritical reynolds numbers [C]. *Proceedings of the 26th*

International Conference on Offshore Mechanics and Arctic Engineering, San Diego, California, USA, 2007, 731-740.

[3] Roddier D., Finnigan T., Liapis S. Influence of the Reynolds number on spar vortex induced motions (VIM): multiple scale model test comparisons [C]. *Proceedings of the 28th International Conference on Offshore Mechanics and Arctic Engineering*, Honolulu, Hawaii, USA, 2009, 797-806.

[4] Rijken O., Leverette S. Field measurements of vortex induced motions of a deep draft semisubmersible [C]. *Proceedings of the International Conference on Offshore Mechanics and Arctic Engineering*. Honolulu, Hawaii, USA, 2009, 739-746.

[5] Ma W., Wu G., Thompson H., et al. Vortex induced motions of a column stabilized floater [C]. *Deep Offshore Technology International Conference*, Houston, Texas, USA, 2013.

[6] Maximiano A., Koop A., de Wilde J. et al. Experimental study on the vortex-induced motions (VIM) of a semi-submersible floater in waves [C]. Trondheim, Norway, 2017.

[7] Waals O. J., Phadke A. C., Bultema S. Flow induced motions of multi column floaters [C]. *26th International Conference on Offshore Mechanics and Arctic Engineering*, San Diego, California, USA, 2007, 669-678.

[8] Gonçalves R. T., Rosetti G. F., Fujarra A. L. C. et al. Experimental study on vortex-induced motions of a semi-submersible platform with four square columns, Part I: Effects of current incidence angle and hull appendages [J]. *Ocean Engineering*, 2012, 54: 150-169.

[9] Gonçalves R. T., Nishimoto K., Rosetti G. F. et al. Experimental study on vortex-induced motions (VIM) of a large-volume semi-submersible platform [C]. *ASME 30th International Conference on Ocean, Offshore and Arctic Engineering*, Rotterdam, The Netherlands, 2011, 1-9.

[10] Liu M., Xiao L., Lu H. et al. Experimental investigation into the influences of pontoon and column configuration on vortex-induced motions of deep-draft semi-submersibles [J]. *Ocean Engineering*. 2016, 123: 262-277.

[11] Gonçalves R. T., Hannes N. H., Chame M. E. F. et al. FIM-flow-induced motions of four-column platforms [J]. *Applied Ocean Research*, 2020, 95: 102019.

[12] Modir A., Mohammadkhani A., Ahani H. Experimental investigation of the flow-induced motion of a square-section cylinder [J]. *Journal of Hydrodynamics*. 2021, 33(2): 301-310.

[13] Chen C. R., Chen H. C. Simulation of vortex-induced motions of a deep draft semi-submersible in current [J]. *Ocean Engineering*, 2016, 118: 107-116.

[14] Liang Y., Tao L. Interaction of vortex shedding processes on flow over a deep-draft semi-submersible [J]. *Ocean Engineering*, 2017, 141: 427-449.

[15] Xu Q., Kim J., Bhaumik T. et al. Validation of HVS semisubmersible VIM performance by model test and CFD [C]. *ASME 31st International Conference on Ocean, Offshore and Arctic Engineering*, Rio de Janeiro, Brazil, 2012, 175-185.

[16] Holland V., Tezdogan T., Oguz E. Full-scale CFD investigations of helical strakes as a means of reducing the vortex induced forces on a semi-submersible [J]. *Ocean Engineering*, 2017, 137: 338-351.

[17] Zhao W., Zou L., Wan D. et al. Numerical investigation of vortex-induced motions of a paired-column semi-submersible in currents [J]. *Ocean Engineering*, 2018, 164: 272-283.

[18] Kim S. J., Spernjak D., Holmes S. et al. Vortex-induced motion of floating structures: CFD sensitivity considerations of turbulence model and mesh refinement [C]. *ASME 34th International Conference on Ocean, Offshore and Arctic Engineering*, St. John's, Newfoundland, Canada, 2015.

[19] Liang Y., Tao L., Xiao L. Energy transformation on flow-induced motions of multiple cylindrical structures with various corner shapes [J]. *Physics of Fluids*, 2020, 32(2): 027105.

[20] Liu Y., Liu F., Wang E. et al. The effect of base column on vortex-induced vibration of a circular cylinder with low aspect ratio [J]. *Ocean Engineering*, 2020, 196: 106822.

[21] Zhao W. W., Wan D. C. Detached-eddy simulation of flow past tandem cylinders [J]. *Applied Mathematics and Mechanics (English Edition)*, 2016, 37(12): 1272-1281.